Original Article

Journal of Intelligent Material Systems and Structures

Journal of Intelligent Material Systems and Structures 2019, Vol. 30(16) 2464–2477 © The Author(s) 2019 Article reuse guidelines: sagepub.com/journals-permissions DOI: 10.1177/1045389X19862383 journals.sagepub.com/home/jim

Experimentally validated model and analytical investigations on power optimization for piezoelectric-based wireless power transfer systems

Binh Duc Truongo, Shane Williams and Shad Roundy

Abstract

This article presents a near-field low-frequency wireless power transfer system utilizing a piezoelectric transducer with magnet tip mass as a receiver. The interaction moment between the uniform **B** field generated by a Helmholtz coil and the magnet is the means to deliver the electrical energy from the transmitter to an electrical load, which is therefore referred to as magneto-mechano-electric effect. This is the first time a complete equivalent circuit model of such a structure is developed and experimentally verified. Based on the lumped model, various aspects of the power optimization problem are thoroughly discussed, providing a comprehensive view of the system and an important premise for further study.

Keywords

wireless power transfer, magneto-mechano-electric effect, lumped-element model, power optimization, impedance matching

I. Introduction

With the rapid development of technology, the Internet of Thing is beginning to shape the future of our modern world in which smart sensing systems require electronics that need not be plugged in or regularly recharged (Zhu et al., 2015; Hassan et al., 2017). Energy harvesting (EH) and wireless power transfer (WPT) hence become promising alternatives to the batteries currently in use (Roundy and Wright, 2004; Beeby et al., 2006; Mitcheson et al., 2008; Erturk et al., 2009; Kurs et al., 2007; Sample et al., 2011; Kiani and Ghovanloo, 2012; Pacini et al., 2017; Song et al., 2017). While the performance of EH systems is strongly dependent on the conditions of the environmental power source (Wei and Jing, 2017), WPT provides deterministic controllable techniques for actively transferring power from an optional source to desired electronic applications (Assawaworrarit et al., 2017; Paul and Sarma, 2018).

For biomedical applications, the amplitude of the magnetic field that can be applied to humans is constrained by the driving frequency due to safety standards (IEEE C95.1-2005, 2006; IEEE C95.6-2002, 2002). For instance, a maximum permissible field at 1 MHz is \approx 200 μ T, while that at 1 kHz is \approx 2mT This

relationship between maximum allowable magnetic field and frequency limits the potential of near-field WPT systems such as capacitive or inductive coupling (Huang et al., 2013; Barman et al., 2015), since the operating frequency of these devices is typically in the range of MHz.

Instead of inducing voltage on a receiver as two resonant inductively coupled coils do, Challa et al. (2012) proposed a near-field WPT system using an electromagnetic transducer to convert the mechanical energy from the oscillating magnet tip mass to electrical energy. The authors focused on analyzing the system efficiency (defined by the ratio of the power delivered to a load and the power input to the network), which may not be a key factor of a low-power system. Meanwhile, the electrodynamic coupling coefficient between the mechanical and electrical domains was not fully

Department of Mechanical Engineering, The University of Utah, Salt Lake City, UT, USA

Corresponding author:

Binh Duc Truong, Department of Mechanical Engineering, The University of Utah, 1495 E. 100 S., 1550 MEK, Salt Lake City, UT 84112, USA. Email: Binh.D.Truong@utah.edu

modeled, and its influence on the mechanical dynamics and maximum output power of the WPT system was not discussed. In related works, other authors reported several experimental observations indicating the potential application of piezoelectric devices for harvesting power from current-carrying conductors or ambient low-frequency magnetic fields (Paprotny et al., 2013; Liu and Dong, 2014; Han et al., 2015). However, the entire model for these designs has not been addressed in a systematic and complete manner.

In the context of WPT, low-frequency systems gain more and more attractions in the last recent years. Garraud et al. (2014) introduced an alternative architecture, in which two torsional springs, a permanent magnet, and a coil were used as a receiver. It should be noted that the inductive coupling between the transmitter and receiver coils was shown to be negligible; the mechanical oscillation of the magnet generated most of the power at the receiver. Later prototypes by the same group demonstrated capabilities of utilizing two transmitting technologies: a coil-based transmitter and a rotating-magnet transmitter (Garraud et al., 2018). Experiments on through-body and multi-receiver transmissions were conducted, opening the way for biomedical implants and wearables. Another concept based on the continuous rotation of the permanent magnet was presented (Garraud et al., 2019). Under steady-state operation, the rotating magnet acts as a synchronous machine rather than a resonant system. This technique enables transferring power over a wide range of frequencies, as opposed to at a particular frequency nearby the mechanical resonance of the receiver.

Based on the Euler-Bernoulli beam theory, the closed-form distributed parameter solutions for piezoelectric EH from base excitations were obtained and thoroughly analyzed for both unimorph and bimorph cantilever configurations (Erturk & Inman, 2011, 2009). Apart from that, this article aims to present an explicit lumped-parameter model, which is widely used for modeling vibration-based energy harvesters and is convenient to approximately describe the behavior of distributed physical systems. For a cantilever beam, if the proof mass to the beam mass ratio is significantly large, the single degree-of-freedom lumped-element model and the distributed parameter model are considerably the same (Erturk and Inman, 2008a, 2008b). The explicit form of the transduction factor and the analytical solution of the power transferred to a load are derived as functions of the device dimensions and the external **B** field. In addition to maximize the transmission efficiency, it is of great interest to understand how to optimize the generated power under different situations. This is therefore one of the central objectives of this

The outline of this article is as follows. First of all, we establish a complete equivalent circuit model of the piezoelectric-based low-frequency wireless power

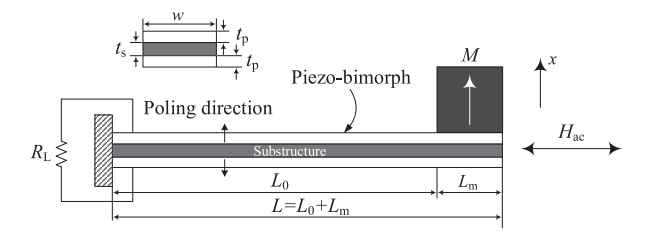


Figure 1. Schematic of MME transducer.

transfer system (WPTS) in section "Mathematical model." We then experimentally validate the developed model in section "Experimental validation." Based on the validated model, sections 4 and 5 further present analytical solutions of the power optimization problem, providing a comprehensive theoretical analysis under different standpoints. Various effects of (i) the thickness ratio constraint, (ii) material properties (e.g. the piezoelectric strain coefficient and Young's modulus of the shim layer), and (iii) the leakage current of the piezoelectric transducer are given in section 6. Section 7 finally summarizes the study.

2. Mathematical model

Figure 1 illustrates the piezoelectric bimorph/magnet magneto-mechano-electric (MME) composite cantilever, including definition of the beam parameters such as w, t_p , t_s , L, L_0 , and L_m . The mechanism that transfers power to the MME transducer is similar to that of a piezoelectric energy harvester; however, it is different from an acoustic WPT system presented in the literature (in which ultrasonic waves are transmitted between two piezoelectric transducers). Assuming that the alternating current (AC) magnetic field $H_{\rm ac}$ of the Helmholtz coil is ideally uniform, a pure moment $M_{\rm B}$ acts on the magnet tip mass M, which is given by Liu and Dong (2014)

$$M_{\rm B} = J_{\rm r} C_{\rm M} H_{\rm ac} \tag{1}$$

where $J_{\rm r}$ is the remanent magnetic polarization and $C_{\rm M}=L_{\rm m}^3$ is the volume of the cubic magnet. Here, the vibration amplitudes are assumed to be small. The equivalent force positioned at the center of mass of $M_{\rm B}$, which results in the same displacement, is (Bucciarelli, 2009)

$$F_{\rm M} = \frac{3}{2} \frac{M_{\rm B}}{l_{\rm eff}} \tag{2}$$

where the effective length is $l_{\rm eff} = (L + L_0)/2$. It should be noted that for the use of thick single-coil (Challa et al., 2012), the moment $M_{\rm B}$ and a force $F_{\rm B}$ co-exist due to the field and the field gradient, respectively. Under such a circumstance, the pure force $F_{\rm B}$ acting on the magnet in the same vibration direction x is (Challa

 $V_{\rm T} = \frac{\Gamma}{C_0} x + \frac{1}{C_0} q$

where $F_{\rm T}$ is the transducer force, $V_{\rm T}$ is the voltage across the terminals of the electric port, $K_1 = K_0 + \Gamma^2/C_0$ is the open-circuit stiffness, C_0 is the clamped capacitance, Γ is the transduction factor, and q is the charge on the positive electrical terminal.

Since the physical model studied in this work has a

tip mass with appreciable length, the distribution of the tip mass over a finite span (i.e. $L_{\rm m}$) is taken into account instead of a concentrated mass model. Adapted from

Kim and Kim (2011), the static deflection shape func-

tion $\phi(y)$ can be expressed as two polynomial functions

corresponding to two portions of the beam with and

(7)

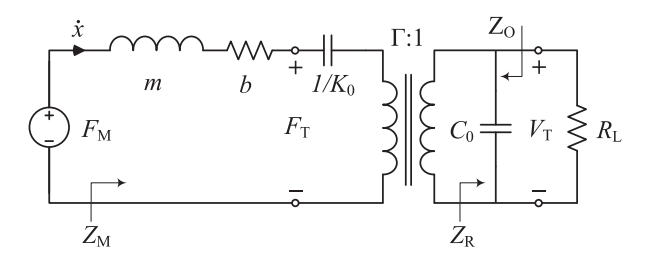


Figure 2. Equivalent two-port model.

et al., 2012) $F_{\rm B} = J_{\rm r} C_{\rm M} (\partial H_{\rm ac}(x)/\partial x)$. The total equivalent force is thus $F = F_{\rm M} + F_{\rm B}$. However, for the current case (i.e. we are considering a uniformed field), $F = F_{\rm M}$ only, and the effect of $F_{\rm B}$ is out of scope of this article. The effective mass of the piezoelectric transducer consisting of the magnet mass M and the beam mass $m_{\rm b}$ is (Rao, 2010, section 2.5)

$$m = M + \frac{33}{140} m_{\rm b} \tag{3}$$

where $m_b = wL(2t_p\rho_p + t_s\rho_s)$ and $M = \rho_M C_M$. ρ denotes the mass density of material. The effective short-circuit stiffness is approximated as (Erturk and Inman, 2011)

$$K_0 = \frac{3(YI)_{\rm c}}{l_{\rm off}^3} \tag{4}$$

where $(YI)_c$ is the flexural rigidity of the composite beam.

without the mass without the mass
$$M$$
 and the beam $0 \le y \le L_0$:
$$(L_m(L_0 + L) \ge L_m \ge 1)$$

 $\phi_{1}(y) = q_{\rm m} \left(\frac{L_{\rm m}(L_{0} + L)}{4} y^{2} - \frac{L_{\rm m}}{6} y^{3} \right)$ $+ q_{\rm b} \left(\frac{L^{2}}{4} y^{2} - \frac{L}{6} y^{3} + \frac{1}{24} y^{4} \right),$ (8)

 $L_0 \leq y \leq L$:

$$\phi_{2}(y) = q_{\rm m} \left(\frac{L_{0}L_{\rm m}L}{2} y - \frac{L_{0}^{2}L_{\rm m}(2L + L_{\rm m})}{12} \right) + q_{\rm b} \left(\frac{L_{0}(L^{2} + L_{0}L_{\rm m} + 2L_{\rm m}^{2})}{6} y - \frac{L_{0}^{2}(L^{2} + 2L_{0}L_{\rm m} + 5L_{\rm m}^{2})}{24} \right)$$

$$(9)$$

where

$$q_{\rm m} = \frac{24}{\left\{L_0 \left[2L_{\rm m} \left(4L_0^2 + 6L_0L_{\rm m} + 3L_{\rm m}^2\right) + q_{\rm r} \left(3L_0^3 + 10L_0^2L_{\rm m} + 12L_0L_{\rm m}^2 + 6L_{\rm m}^3\right)\right]\right\}}, \quad (10)$$

 $q_{\rm b} = q_{\rm m}q_{\rm r},\tag{11}$

$$q_{\rm r} = \frac{L_{\rm m} m_{\rm b}}{LM}.$$
 (12)

Depending on whether the wiring is in parallel or series (Erturk and Inman, 2011), C_0 and Γ are evaluated differently. For the case of series connection

$${}^{S}C_{0} = \frac{1}{2} \epsilon_{33}^{S} \frac{wL}{t_{p}},$$

$${}^{S}\Gamma = -e_{31}w \frac{t_{p} + t_{s}}{2} \frac{d\phi_{1}(y)}{dy} \bigg|_{y = L_{0}}$$

$$= \frac{-2e_{31}w(t_{p} + t_{s})(3(M + m_{b})L^{2} - 3m_{b}L_{0}L + m_{b}L_{0}^{2})}{(6(M + m_{b})L^{3} - 6m_{b}L_{0}L^{2} + 2L_{0}^{2}L(M + 2m_{b}) - L_{0}^{3}m_{b})}$$

$$(14)$$

where ϵ_{33}^{S} is the permittivity component at constant strain with the plane-stress assumption of a thin beam (i.e. $\epsilon_{33}^{S} = \epsilon_{33}^{T} - d_{31}^{2}/s_{11}^{E}$ where d_{31} is the piezoelectric strain constant, s_{11}^{E} is the elastic compliance at constant electric field, and ϵ_{33}^{T} is the permittivity component at

The expression of $(YI)_c$ for bimorph configuration is (Roundy and Wright, 2004)

$$(YI)_{c} = 2Y_{p} \left[\frac{wt_{p}^{3}}{12} + wt_{p} \left(\frac{t_{s} + t_{p}}{2} \right)^{2} \right] + Y_{s} \frac{wt_{s}^{3}}{12}$$
 (5)

where Y_p and Y_s are the elasticity constants of the piezoelectric layers and the substructure, respectively. The coupling between the electrical and mechanical domain is conveniently modeled as a linear two-port transducer, as depicted in Figure 2, where b is the mechanical damping coefficient and the electrical load is simply represented by a resistance R_L . The linear two-port equations for the piezoelectric transducer can be written as follows (Tilmans, 1996; Halvorsen, 2016)

$$F_{\rm T} = K_1 x + \frac{\Gamma}{C_0} q,\tag{6}$$

constant stress). e_{31} is the effective piezoelectric stress constant, which can be given as $e_{31} = d_{31}/s_{11}^{E}$ based on the same assumption.

For the case of parallel connection

$${}^{P}C_{0} = 4^{S}C_{0}, (15)$$

$${}^{P}\Gamma = 2^{S}\Gamma. \tag{16}$$

It should be noted that the output power is independent of series/parallel configurations.

With a time harmonic drive force $F_{\rm M}(t) = F_0 \cos{(\omega t)}$ of angular frequency ω and a resistance $R_{\rm L}$ directly connected to the electrical ports, the transverse velocity of the tip mass $U_{\rm m}$ and the output voltage $V_{\rm T}$ can be derived from the equivalent circuit model as

$$U_{\rm m} = \frac{F_0}{Z_{\rm M}},\tag{17}$$

$$V_{\rm T} = \frac{F_0 - \left(j\omega m + \frac{K_0}{j\omega} + b\right)U_{\rm m}}{\Gamma} \tag{18}$$

where the impedance $Z_{\rm M}$ reads as

$$Z_{\rm M} = \left(j\omega m + \frac{K_0}{j\omega} + b\right) + \Gamma^2 Z_{\rm R},\tag{19}$$

$$Z_{\rm R} = \frac{\frac{1}{j\omega C_0} R_{\rm L}}{\frac{1}{j\omega C_0} + R_{\rm L}} = \frac{R_{\rm L}}{1 + j\omega R_{\rm L} C_0}.$$
 (20)

The power transferred to the load is then given by

$$\begin{split} P &= \frac{1}{2} \frac{|V_{\rm T}|^2}{R_{\rm L}} \\ &= \frac{1}{2} \frac{\Gamma^2 F_0^2}{R_{\rm L}} \frac{|Z_{\rm R}|^2}{|Z_{\rm M}|^2} = \frac{1}{2} \Delta K \frac{\omega^2 \tau}{1 + (\omega \tau)^2} \frac{F_0^2}{(\omega |Z_{\rm M}|)^2} \\ &= \frac{1}{2} \Delta K \frac{\omega^2 \tau}{1 + (\omega \tau)^2} F_0^2 / \\ &\left\{ \left[\omega b + \Delta K \frac{\omega \tau}{1 + (\omega \tau)^2} \right]^2 + \left[K_1 - m \omega^2 - \Delta K \frac{1}{1 + (\omega \tau)^2} \right]^2 \right\} \end{split}$$

$$(21)$$

where the electrical time scale is $\tau = R_L C_0$; the difference between the highest and the lowest mechanical stiffness is denoted as $\Delta K = \Gamma^2/C_0$ and $|X_0| = F_0/(\omega|Z_M|)$ is the displacement amplitude of the tip mass. Formula (21) is the main objective to validate the model, where the frequency and **B**-field responses are the two most important aspects.

3. Experimental validation

Figure 3 shows the experimental setup, in which the circular Helmholtz coils are used as a transmitter. The

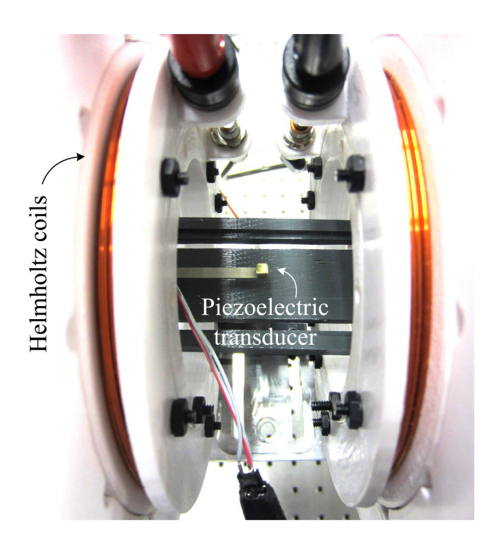


Figure 3. Experiment setup, in which a circular Helmholtz coil is used as a transmitter and the magnet tip mass of a piezoelectric-based receiver is placed at the center of the coil.

Table I. Model parameters.

| π×10 ⁻⁷ H/m .175 mm 9.7 mm .14 mm 6×10 ⁹ Pa -190×10 ⁻¹² m/V .56 nF 800 kg/m ³ .1 mm 00×10 ⁹ Pa 500 kg/m ³ .175 mm 630 kg/m ³ .45 T .13×10 ⁻³ N s/m .03% 8.5 |
|---|
| |

PZT: lead zirconate titanate.

generated **B** field is obtained using an AC milligauss meter (i.e. which is in root mean square (RMS) equivalent units). The receiver consists of a bimorph PZT-5A4E cantilever beam with a permanent magnet attached at its tip which is located in the center of the two coils. The Helmholtz coils are controlled by a Tektronix function generator connecting to a Rigol power amplifier. The induced voltage across the load resistance is measured by a laptop oscilloscope and the average output power is then computed as $P = \frac{1}{T} \int_0^T (V_T^2(t)/R_L) dt$. The mechanical damping coefficient b is determined by fitting the model to the experiment with $B = 40.5\sqrt{2} \,\mu\text{T}$ and $R_L = 1 \,\text{M}\Omega$. The model parameters are now given and listed in Table 1, which is then used for validating all the following cases.

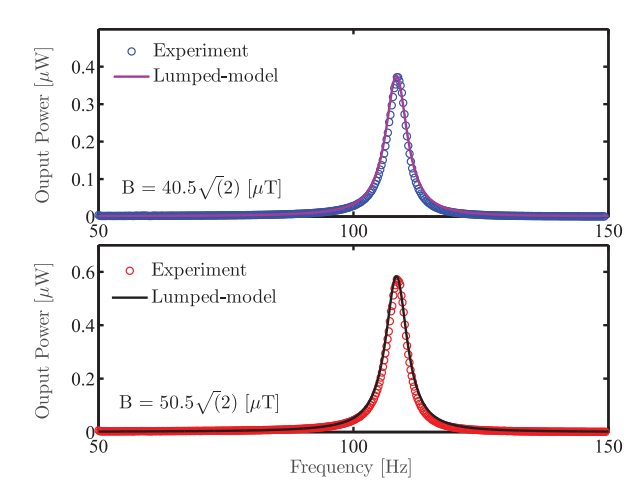


Figure 4. Frequency response comparisons between the experimental data and simulation results by the model.

Figure 4 shows a good agreement between the model results and the measurements for both $B = 40.5\sqrt{2} \,\mu\text{T}$ and $50.5\sqrt{2} \,\mu\text{T}$ when the drive frequency is swept from 50 to 150 Hz over a time duration of 40 s. Note that 40.5 and 50.5 are RMS values measured by the AC milligauss meter. The load resistance is $R_{\rm L} = 1 \text{ M}\Omega$ and the corresponding optimal frequency is experimentally found at about $f_r = 108.5 \,\mathrm{Hz}$. Increase in the input magnetic field strength results in stronger moment acting on the magnet tip mass and therefore higher power delivered to the load. Figure 5 shows that the accuracy of the model is consistent when the applied magnetic flux density amplitude is discretely varied from 0 up to $B = 89.5 \,\mu\text{T}$. The load resistance is kept the same as that of in Figure 4 and the drive frequency is fixed at $f_{\rm r} = 108.5 \, {\rm Hz}$. The transferred power obtained from experiments and simulations are almost identical, which is a quadratic function in terms of the **B**-field amplitude. In summary, the lumped model has successfully predicted the two most important behavior that are frequency response and magnetic field response.

4. Power optimization principles: gradient descent method

We now utilize the developed model to further investigate the power optimization problem at a given applied **B** field with respect to the load and the drive frequency for different possible cases. This is of interest not only from the mathematical point of view but also to provide a complete physical insight of the WPT system.

Case I. At $\omega = \omega_0 = \sqrt{K_0/m}$, the optimal load and the corresponding optimum output power are given by

$$R_{\rm L}^{\rm opt}|_{\omega = \omega_0} = \frac{1}{\omega_0 C_0 \sqrt{M_0^2 + 1}},$$
 (22)

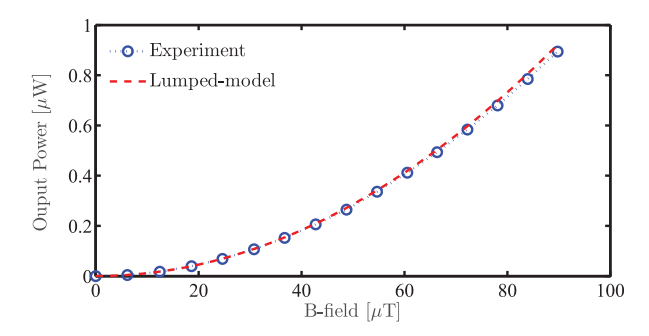


Figure 5. Comparisons of the external **B**-field responses between the model simulations and experiments with $R_1 = 1 \text{ M}\Omega$ and $f_r = 108.5 \text{ Hz}$.

$$P^{\text{opt}}|_{\omega = \omega_0} = \frac{F_0^2}{4b} M_0 \left(\sqrt{M_0^2 + 1} - M_0 \right).$$
 (23)

Here, the resonator figure of merit is defined as $M_f = \Delta K/(b\omega)$ (Vittoz, 2010). In particular, at the resonant frequency $M_0 = \Delta K/(b\omega_0)$.

Case II. At
$$\omega = \omega_1 = \sqrt{K_1/m}$$
, we get

$$R_{\rm L}^{\rm opt}|_{\omega = \omega_0} = \frac{\sqrt{M_1^2 + 1}}{\omega_1 C_0},$$
 (24)

$$P^{\text{opt}}|_{\omega = \omega_0} = \frac{F_0^2}{4b} M_1 \left(\sqrt{M_1^2 + 1} - M_1 \right)$$
 (25)

where $M_1 = \Delta K/(b\omega_1)$. In general, $P^{\rm opt}|_{\omega = \omega_0}$ and $P^{\rm opt}|_{\omega = \omega_1}$ are not identical; however, for moderately coupled systems $M_0 \approx M_1$, the two maximum powers approximately coincide.

Case III. The solution of the optimal load considered as a function of the drive frequency and the other system parameters is calculated by

$$R_{\rm L}^{\rm opt}|_{\omega} = \frac{1}{\omega C_0} \sqrt{\frac{(K_0 - m\omega^2)^2 + (\omega b)^2}{(K_1 - m\omega^2)^2 + (\omega b)^2}}.$$
 (26)

We can observe that equation (26) reduces to equations (22) and (24) when $\omega = \omega_0$ and $\omega = \omega_1$ correspondingly.

Case 4. We now treat $\tau = R_L C_0$ as a constant (i.e. R_L is kept fixed) and consider ω to be a variable parameter. This investigation is motivated by the fact that the drive frequency can be easily subjected to control in WPT systems. Similarly, the stationary points of the power are determined by $dP/d\omega = 0$ or equivalently

$$2m\tau^2\omega^6 + \omega^4(b^2\tau^2 + m^2 - 2K_1m\tau^2) - K_0^2 = 0.$$
 (27)

The (real) optimal frequency is derived as follows

$$\omega^{\text{opt}} = \left[\frac{1}{3\lambda_1} \left(\frac{\Lambda}{\sqrt[3]{2}} + \frac{\sqrt[3]{2}\lambda_2^2}{\Lambda} - \lambda_2 \right) \right]^{1/2}$$
 (28)

where

$$\lambda_1 = 2(m\tau)^2,\tag{29}$$

$$\lambda_2 = b^2 \tau^2 + m^2 - 2K_1 m \tau^2, \tag{30}$$

$$\Lambda = \left(27(\lambda_1 K_0)^2 - 2\lambda_2^3 + 3\sqrt{3}(\lambda_1 K_0)\sqrt{27(\lambda_1 K_0)^2 - 4\lambda_2^3}\right)^{1/3}.$$
(31)

Figure 6 shows a comprehensive picture of the transferred power with respect to the normalized angular frequency ω/ω_0 and the load resistance $R_{\rm L}$. The corresponding power obtained by using equation (28) is also included, which is the maximum transferable power at each value of $R_{\rm L}$.

Case V. Finally, we consider the condition in which both the load resistance $R_{\rm L}$ (and therefore, the parameterized time constant τ) and the drive frequency ω are simultaneously considered as objective control variables. Stationary point(s) of the general power optimization problem are given by solving ${\rm d}P/{\rm d}\tau=0$ and ${\rm d}P/{\rm d}\omega=0$ simultaneously. Substituting the optimal time constant $\tau^{\rm opt}=R_{\rm L}^{\rm opt}C_0$ from equation (26) into equation (27), the latter equation reduces to

$$3\omega^8 - 4\alpha\omega^6 + (\alpha^2 + 2\beta)\omega^4 - \beta^2 = 0$$
 (32)

where

$$\alpha = (\omega_0^2 + \omega_1^2)(1 - 4\zeta_e^2), \tag{33}$$

$$\beta = (\omega_0 \omega_1)^2, \tag{34}$$

$$\zeta_{\rm e} = \frac{b}{2\sqrt{m(K_0 + K_1)}}. (35)$$

Equation (32) can be rewritten as

$$\left[\omega^2(2\omega^2 - \alpha)\right]^2 = \left(\omega^4 - \beta\right)^2,\tag{36}$$

which results in three (positive) distinguished solutions

$$\omega_{\rm m} = \left[\frac{\alpha + \sqrt{\alpha^2 + 12\beta}}{6} \right]^{1/2},\tag{37}$$

$$\omega_{\mathbf{M}_1} = \left[\frac{\alpha - \sqrt{\alpha^2 - 4\beta}}{2} \right]^{1/2},\tag{38}$$

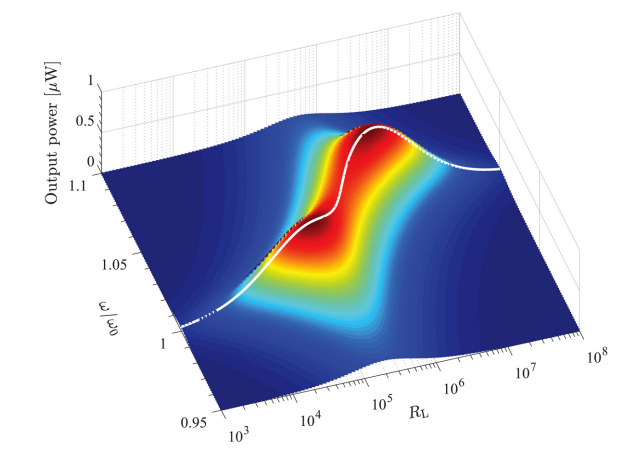


Figure 6. Output power as a function of driving frequency and load resistance. White solid line: corresponding power with analytical solution of the optimal frequency expressed in equation (28).

$$\omega_{\rm M_2} = \left[\frac{\alpha + \sqrt{\alpha^2 - 4\beta}}{2} \right]^{1/2}.\tag{39}$$

Here, ω_{M_1} and ω_{M_1} are real if and only if $\zeta_e \in \{(0,\zeta_1] \cup [\zeta_2, +\infty]\}$, where

$$\zeta_1^2 = \frac{1}{4} \frac{(\omega_1 - \omega_0)^2}{\omega_0^2 + \omega_1^2},\tag{40}$$

$$\zeta_2^2 = \frac{1}{4} \frac{(\omega_1 + \omega_0)^2}{\omega_0^2 + \omega_1^2}.$$
 (41)

The condition $\zeta_e \leq \zeta_1$ is equivalent to

$$k^2 \ge k_{\rm cr}^2 = 1 - \frac{1}{(2\zeta_0 + 1)^2}$$
 (42)

where the squared electromechanical coupling factor $0 \le k^2 \le 1$ and the damping ratio ζ_0 at the short-circuit resonant frequency ω_0 are given by

$$k^2 = \frac{\Gamma^2}{K_1 C_0},\tag{43}$$

$$\zeta_0 = \frac{b}{2\sqrt{mK_0}} = \frac{b}{2m\omega_0}. (44)$$

Meanwhile, $\zeta_e \ge \zeta_2$ leads to $1 - k^2 > 1/(1 - 2\zeta_0)^2 > 1$, which cannot occur. Equation (36) has a unique positive solution $\omega_{\rm m}$ when the coupling is lower than critical, $k^2 < k_{\rm cr}^2$. Therefore, the optimum output power in this case is attained at $\omega_{\rm m}$. However, this power is less than the maximum achievable power when $k^2 \ge k_{\rm cr}^2$. See Shu et al. (2007), Arroyo et al. (2012), and Liao and Sodano (2018) for an example. Note that the corresponding optimal load is computed by substituting the

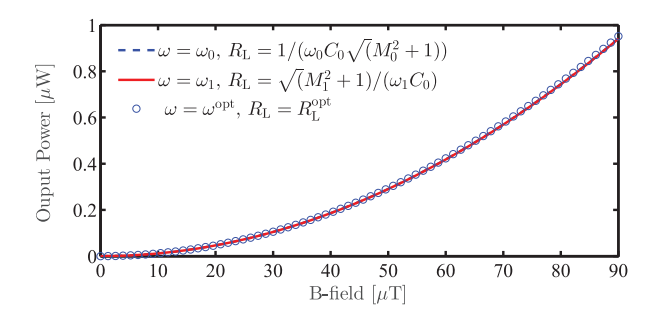


Figure 7. Maximum transferred power at different optimal conditions (*Cases I, II*, and *V*).

optimal frequency back into equation (26). The accuracy of these calculations is confirmed by an independent numerical method in Appendix 3.

In the currently studied device, the maximal power points achieved from *Cases I, II*, and V are considerably the same as depicted in Figure 7. However, we also found that in some circumstances, the maximum powers in *Cases I* and *II* can drop down to 95% or 92%, respectively, when compared to that of *Case V*. An example is discussed in Appendix 3 in which b, Γ , L, and t_p are mathematically adjusted for proving the statement. Supporting information for *Cases I, II, III, IV*, and V can also be found in Appendices 1 to 3.

5. Power optimization principles: impedance matching

In addition to the gradient descent method, impedance matching is a powerful approach for determining the condition of system parameters under which the power transferred to the load is maximized. We have shown that for an inductively coupled WPT system, the simultaneous optimization of load resistance and driving frequency generates almost identical output power compared to the case where the resonator impedance is matched to a particular load (Truong, 2019). However, a single-end conjugate-matched circuit at either source or load does not result in maximum power transfer through a physical two-port network in general. In other words, power delivered to a load is maximized by simultaneous conjugate matching at both ends (source and load; Truong, 2019). These findings lead to a question of how the piezoelectric-magnet WPT system performs under different conjugate matching conditions. In this section, solutions of impedance matching problems in comparison with the results presented in section 4 are addressed.

5.1. Impedance matching to the load

From the equivalent circuit model shown in Figure 2, the output impedance Z_0 is calculated as

$$Z_{\rm O} = \frac{\frac{1}{j\omega C_0} \left[\frac{1}{\Gamma^2} \left(j\omega m + \frac{K_0}{j\omega} + b \right) \right]}{\frac{1}{j\omega C_0} + \left[\frac{1}{\Gamma^2} \left(j\omega m + \frac{K_0}{j\omega} + b \right) \right]}.$$
 (45)

Based on the impedance matching technique shown in Challa et al. (2012), the optimal load is given by

$$R_{\rm L}^{\rm opt} = |Z_{\rm O}| = \frac{1}{\omega C_0} \sqrt{\frac{(K_0 - m\omega^2)^2 + (\omega b)^2}{(K_1 - m\omega^2)^2 + (\omega b)^2}},$$
 (46)

which is the same as in equation (26) (Case III).

Given the fact that the formula $R_{\rm L}^{\rm opt} = |Z_{\rm O}|$ does not fully reflect the maximum power transfer theorem followed by the impedance matching condition $Z_{\rm L} = Z_{\rm O}^*$ (Kong, 1995; here, $Z_{\rm L}$ denotes the general load impedance), we now consider the complete case where $\Im\{Z_{\rm O}\} = 0$ and $R_{\rm L} = \Re\{Z_{\rm O}\}$. The former equation results in

$$\omega_{-} = \left[\frac{\omega_0^2 + \omega_1^2}{2} + \frac{\kappa - b^2}{2m^2} \right]^{1/2},\tag{47}$$

$$\omega_{+} = \left[\frac{\omega_0^2 + \omega_1^2}{2} - \frac{\kappa + b^2}{2m^2} \right]^{1/2} \tag{48}$$

where

$$\kappa^2 = [(m(\omega_0 + \omega_1))^2 - b^2][(m(\omega_0 - \omega_1))^2 - b^2]. \quad (49)$$

The latter equation yields

$$R_{\rm L} = \frac{\Delta K}{C_0} \frac{b}{(K_1 - m\omega^2)^2 + (\omega b)^2}.$$
 (50)

We find that $\omega_- = \omega_{\rm M_1}$ and $\omega_+ = \omega_{\rm M_2}$ and the optimum power obtained by the two methods (complete impedance matching to the load, and gradient algorithm *Case V*) are identical.

An attempt to maximize the generated power for a piezoelectric energy harvester with the presence of an additional inductor $L_{\rm a}$ in parallel/series with the load resistance $R_{\rm L}$ was proposed in Renno et al. (2009). However, this method is not appropriate in practice since it leads to the optimal inductance in the range of a few H, not yet to mention that its high parasitic resistance may significantly reduce the power delivered to the load.

5.2. Bi-conjugate impedance matching

The equivalent circuit model in Figure 2 can be generalized for any lossless two-port network as shown in Figure 8. The applied force $F_{\rm M}$ and the mechanical damping coefficient b form an effective power source for the two-port network whose output port is connected to a load resistance $R_{\rm E}$ in the later stage. Given a constant amplitude of the applied magnetic flux

Truong et al. 247 l

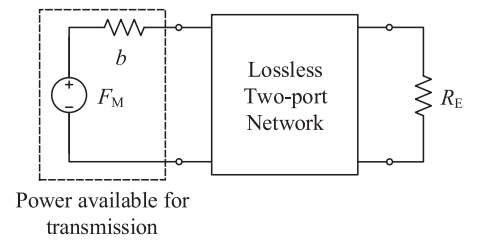


Figure 8. Generalized equivalent circuit model for any lossless two-port network.

density, based on the two-port theory (Gonzalez, 1996), the power available for transmission is determined by

$$P_{\text{avs}} = \frac{1}{8} \frac{F_0^2}{h}.$$
 (51)

In other words, P_{avs} is the largest possible power that can be delivered to the two-port network and therefore is the power limit transferred into the load. Without loss of generality, we consider a lossless network formed by reactances jX and jY as shown in Figure 9. The source, input, output, and load impedances are

$$Z_{\rm s} = b, \tag{52}$$

$$Z_{\rm in} = jX + \frac{jYR_{\rm E}}{iY + R_{\rm E}},\tag{53}$$

$$Z_{\text{out}} = \frac{jY(b+jX)}{b+i(X+Y)},\tag{54}$$

$$Z_{\rm L} = R_{\rm E} \tag{55}$$

respectively. The output voltage and power induced in the load R_E are computed as

$$V_{\rm E} = F_0 \frac{jYR_{\rm E}}{(bR_{\rm E} - XY) + j(bY + XR_{\rm E} + YR_{\rm E})},$$
 (56)

$$P_{\rm E} = \frac{1}{2} \frac{|V_{\rm E}|^2}{R_{\rm E}} = \frac{1}{2} F_0^2 Y^2 R_{\rm E} /$$

$$\left[(bR_{\rm E} - XY)^2 + j(bY + XR_{\rm E} + YR_{\rm E})^2 \right]$$
(57)

and

$$P_{\rm E, lim} = P_{\rm avs}$$
.

The bi-conjugate impedance matching conditions are $Z_{\text{in}} = Z_{\text{s}}^*$ and $Z_{\text{out}} = Z_{\text{L}}^*$, which leads to

$$\Im\{Z_{\rm in}\} = \Im\{Z_{\rm out}\} = 0,$$
 (58)

$$\Re\{Z_{\rm in}\} = \frac{Y^2 R_{\rm E}}{Y^2 + R_{\rm E}^2} = b,\tag{59}$$

$$\Re\{Z_{\text{out}}\} = \frac{Y^2b}{(X+Y)^2+b^2} = R_{\text{E}}.$$
 (60)

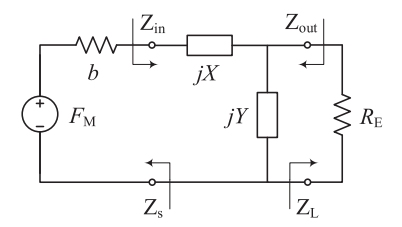


Figure 9. A circuit model with reactance two-port network.

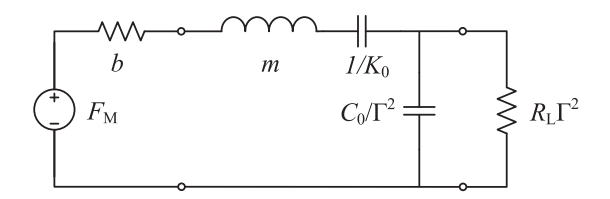


Figure 10. An equivalent circuit of the linear two-port model.

Equation (58) is equivalent to

$$X(R_{\rm E}^2 + Y^2) + YR_{\rm E}^2 = 0, (61)$$

$$b^2 + X(X+Y) = 0. (62)$$

Since X and Y must have opposite sign (XY < 0), one possible solution with Y < 0 is

$$X = \sqrt{b(R_{\rm E} - b)},\tag{63}$$

$$Y = -\frac{R_{\rm E}\sqrt{b}}{\sqrt{R_{\rm E} - b}} \tag{64}$$

with the assumption that $R_E > b$. Surprisingly, these solutions of X and Y also satisfy the other two conditions (equations (59) and (60)). Therefore, equations (63) and (64) are the final solution of the bi-conjugate impedance matching problem. Substituting equations (59) and (60) into equation (57), the optimum power transferred to the load is

$$P_{\rm E}|_{\rm opt} = \frac{1}{8} \frac{F_0^2}{b} = P_{\rm E, lim}.$$
 (65)

We have proved that the limitation of the output power is reached by a bi-conjugate impedance matched system. In general, this conclusion holds for any lossless two-port network.

We then apply the analysis above to the particular piezoelectric resonator used in this article which is assumed to be a lossless transducer. Using the reflected impedance technique (Orfanidis, 2016), the linear two-port model in Figure 2 can be represented by an equivalent circuit depicted in Figure 10. Letting $X = \omega m - K_0/\omega$, $Y = -\Gamma^2/(\omega C_0)$, and $R_E = R_L \Gamma^2$, we recover the case explored in Figure 9. Note that the power in equation (21) is the same as the power

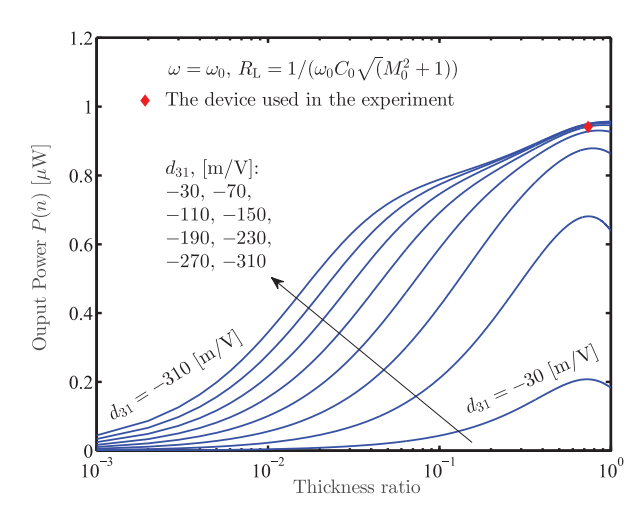


Figure 11. Maximum transferred power as a function of the thickness ratio $n=2t_{\rm p}/t_0$ with different values of d_{31} . The total thickness of the composite laminate t_0 is kept fixed $t_0=0.38$ mm and $Y_{\rm s}=100$ GPa (see Table 1).

delivered to the reflected resistance $R_L\Gamma^2$. Expressions (63) and (64) are written in terms of two variables R_L and ω as follows

$$R_{\rm L} = \frac{1}{bC_0} \left(m - \frac{K_0}{\omega^2} \right),\tag{66}$$

$$\omega^{2} \left(m - \frac{K_{0}}{\omega^{2}} \right)^{2} - \Delta K \left(m - \frac{K_{0}}{\omega^{2}} \right) + b^{2} = 0.$$
 (67)

Equation (67) has two solutions that are identical to equations (47) and (48). The corresponding maximum output power is exactly equal to $P_{\rm E, \, lim}$.

Up to this point, we are able to conclude that three approaches (1) optimal load and frequency by the gradient descent analysis, (2) impedance matching to the load, and (3) bi-conjugate impedance matching collapse to the same solution, in which the output power attains the maximum transferable power (for a given applied magnetic field). The same result was observed for vibration energy harvesters under displacement-unconstrained operation (Renaud et al., 2012; Halvorsen et al., 2013). From a physics standpoint, optimizing the load and frequency in this circumstance is fully equivalent to applying the bi-conjugate impedance matching principle to the piezoelectric-based WPT system under investigation. This conclusion does not always hold true in general. With a lossy two-port network, such as a two-coil magnetically coupled resonator, optimal load and frequency is not able to reach the maximum possible power. Additional impedance matching circuits are required for maximizing the output power to the load. See Heebl et al. (2014) and Kim et al. (2015) for examples.

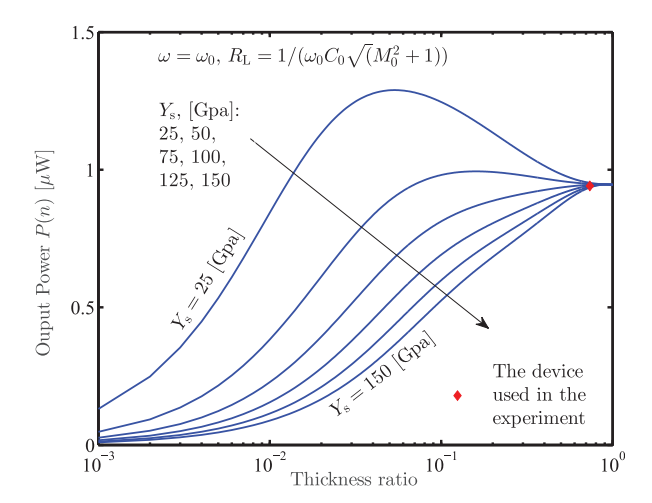


Figure 12. Maximum transferred power as a function of the thickness ratio $n=2t_{\rm p}/t_0$ with different values of $Y_{\rm s}$. The total thickness of the composite laminate t_0 is kept fixed.

6. Discussion

6.1. Thickness ratio-constrained operation

Many researchers are focused on improving the performance of piezoelectric materials. However, constraints on the geometry of the device are also important. Geometric constraints may not be problematic for macro-scale prototypes because the dimensions of the beam (i.e. piezoelectric and substrate layers) are easily controllable. However, in the case of microfabricated generators, where the thickness ratio between piezoelectric and substrate layers is constrained by microfabrication technologies, the power output could be significantly affected. Figure 11 depicts the variations in the generated power with the changes in the thickness ratio defined as $n = 2t_p/t_0$, while the total thickness t_0 and the other parameters are unchanged. The optimal thickness ratio slightly changes with the decrease in $|d_{31}|$, for instance, $n^{\text{opt}} \approx 0.73$ with $d_{31} = -30$ m/V and $n^{\text{opt}} \approx 0.91$ with $d_{31} = -190 \text{ m/V}$. Furthermore, the maximum output power (obtained at corresponding n^{opt}) is nearly saturated with $|d_{31}| \ge 190 \text{ m/V}$ for relatively large n (in particular, $n \ge 0.2$). Here, we assume that the mechanical damping coefficient is nearly unchanged. This assumption is reasonable since the air damping mainly depends on the ambient pressure and the beam length and width (which are kept fixed in this case).

6.2. Material properties

In addition to the piezoelectric strain constant d_{31} , the elastic Young's modulus of the shim Y_s also has a strong influence on both the optimal thickness ratio and the generated power. This issue has not been fully explored in the literature. Figure 12 shows the

dependencies of P^{opt} and n^{opt} on Y_s , in which P^{opt} increases and n^{opt} reduces with the decrease in Y_s . For instance, at an elastic modulus of $Y_s = 100 \text{ GPa}$, $P^{\text{opt}} = 0.95 \,\mu\text{W}$ and $n^{\text{opt}} = 0.909$, while those at $Y_{\rm s} = 25 \text{ GPa are } P^{\rm opt} = 1.29 \text{ } \mu\text{W} \text{ and } n^{\rm opt} = 0.053. \text{ In a}$ general trend, lower Y_s results in higher power transferred to the load at the same thickness ratio. Here, the total thickness and the mechanical quality factor at short-circuit resonant frequency of the composite laminate are kept fixed, $t_0 = 0.38$ mm and $Q_0 = 48.5$ (taken from Table 1). The damping coefficient is calculated by $b = \sqrt{mK_0}/Q_0$. This observation can explain the experimental results reported in Annapureddy et al. (2016, 2018) where an optimum power obtained by a Fe-Ga MME generator was approximately 430% higher than that of a Ni-based MME prototype. Both devices have a similar structure and dimensions. The increase is due to the fact that Young's modulus of Nickel at the room temperature is higher than that of Fe-Ga, $^{\text{Ni}}Y_{\text{s}} \approx 200 \text{ GPa}$ (Luo et al., 2004) in comparison with Fe-Ga $Y_s \approx 140$ GPa (Li et al., 2018). If we choose to keep b fixed and express Q_0 as a function of b, the same trend is observed.

6.3. Leakage current and effective figure of merit

In practice, piezoelectric transducers may have leakage current that cannot be neglected. This parasitic loss is modeled as a resistance connected in parallel with the clamped capacitance of the piezoelectric generator (Arroyo et al., 2012; Halvorsen, 2016). The power delivered to the resistive load now becomes

$$P_{\rm L} = \frac{1}{2} \left(1 - \frac{\tau}{\tau_{\rm p}} \right) \frac{\Delta K \omega^2 \tau}{1 + (\omega \tau)^2} \frac{F_0^2}{(\omega |Z_{\rm M} + b|)^2}$$
(68)

where

$$Z_{\rm M} = j \left(m\omega - \frac{K_0}{\omega} \right) + \Delta K \frac{\tau}{1 + j\omega \tau}, \tag{69}$$

$$\tau_{\rm L} = R_{\rm L} C_0, \ \tau_{\rm p} = R_{\rm p} C_0, \frac{1}{\tau} = \frac{1}{\tau_{\rm L}} + \frac{1}{\tau_{\rm p}}.$$
 (70)

With arbitrary operating frequencies, the optimal load is

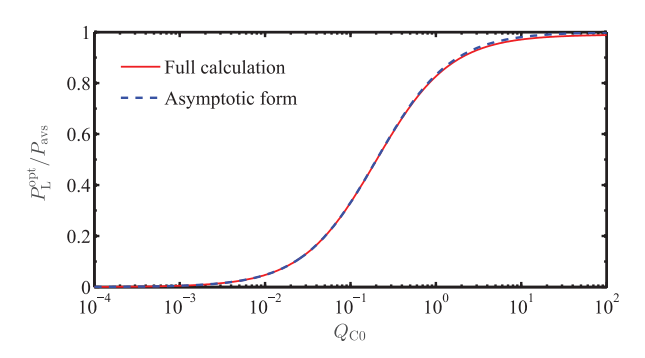


Figure 13. Solutions of the ratio between the optimum output power P_L^{opt} and its limit P_{avs} as functions of Q_{C0} , computed by equations (74) and (75), respectively.

Since $\Delta K = k^2 K_1$, we can write $M = k^2 Q_1 \omega_1/\omega$ or $M = k_{\rm e}^2 Q_0 \omega_0/\omega$, where the Q factors are $Q_0 = m\omega_0/b$ and $Q_1 = m\omega_1/b$, and the expedient coupling coefficient is $k_{\rm e}^2 = k^2/(1-k^2)$. Denoting $M|_{\omega = \omega_0} = M_0$, we have $M_0 = \Delta K/(\omega_0 b) = k_{\rm e}^2 Q_0$. By introducing the electrical quality factor, $Q_{\rm C0} = \omega_0 \tau_{\rm p}$, equation (72) results in

$$\tau_{\rm L}^{\rm opt} = \frac{\tau_{\rm p}}{\sqrt{(M_{\rm e} + 1)^2 + Q_{\rm C0}^2}}.$$
 (73)

The effective (overall) figure of merit is defined by $M_e = M_0 Q_{C0} = k_e^2 Q_0 Q_{C0}$. The optimum delivered power is

$$P_{\rm L}^{\rm opt} = \frac{1}{8} \frac{F_0^2}{b} \frac{2M_{\rm e}}{M_{\rm e} + 1 + \sqrt{(M_{\rm e} + 1)^2 + Q_{\rm C0}^2}}.$$
 (74)

For moderate or high coupling, $M_e \gg Q_{C0}$, and the asymptotic form of the maximum transferable power is

$$P_{\rm L}^{\rm opt} \approx P_{\rm avs} \frac{M_{\rm e}}{M_{\rm e} + 1}$$
 (75)

When $R_p \to \infty$ ($\tau_p \to \infty$), both equations (74) and (75) collapse to the case without the parasitic resistance as shown in equation (65).

The effects of the electrical quality factor Q_{C0} on the optimal output power are depicted in Figure 13. Other

$$\tau_{\rm L}^{\rm opt} = \frac{\tau_{\rm p} \Big[(K_0 - m\omega^2)^2 + (\omega b)^2 \Big]^{1/2}}{\Big[(K_0 - m\omega^2)^2 + (K_1 - m\omega^2)^2 + (\omega b)^2 \Big(1 + (\omega \tau_{\rm p})^2 \Big) + 2\Delta K (\omega^2 b \tau_{\rm p}) \Big]^{1/2}}.$$
 (71)

At resonance frequency $\omega = \omega_0$, equation (71) reduces to

$$\tau_{\rm L}^{\rm opt} = \frac{1}{\omega_0} \frac{1}{\sqrt{1 + (M_0 + 1/(\omega_0 \tau_{\rm p}))^2}}.$$
(72)

parameters such as the coupling coefficient k = 0.3 and the mechanical quality factor $Q_0 = 48.5$ are taken from Table 1. In this particular case, the discrepancy between equations (74) and (75) is negligible. The question on

how to determine R_p (and therefore Q_{C0}) is out of scope of this article.

6.4. Transmission efficiency

Although the efficiency is not a key factor of a lowpower system (e.g. sensor nodes or wearable/implantable applications), it is still of interest to study. We found that the transmission efficiency of the MME configuration is relatively low in comparison with other WPT system such as inductively coupled resonators (Truong and Roundy, 2018). Despite this obvious drawback, an advantage of the MME system is that the applied magnetic field can be higher at the low frequencies required by the MME system while still remaining within safe limits. According to the IEEE standards, a maximum allowable field at 1 kHz is 2 mT, 10 times larger than the 200 μ T permissible at 1 MHz (IEEE C95.1-2005, 2006; IEEE C95.6-2002, 2002). In the case that the receiver is blocked by a metal plate, high-frequency devices such as inductive/capacitive coupled systems cannot be utilized due to the effects of eddy currents (i.e. also called Foucault currents, which flow in closed loops within conductors and in planes perpendicular to the applied magnetic field).

7. Conclusion

The main aim of this work was to present an experimentally validated lumped-parameter model for a piezoelectric-based WPT system, providing thorough analyses on how to optimize the delivered power and reveal the essential role of the device thickness ratio. The electromechanical transduction factor was given as an explicit formula of device geometry, rather than a derivative (or integral) function reported in the literature. The solution of the optimal load at the resonance/ anti-resonance frequency (Case I/II), the general optimal load at an arbitrary frequency (Case III), the optimal driving frequency with respect to the load (Case IV), and the simultaneous optimal load and frequency (Case V) were analytically derived in explicit forms. It was shown that for the system under consideration, optimizing the load and frequency is equivalent to biconjugate impedance matching. The fundamental maximum transferable power for a given external B field was revealed, which can be reached by concurrently tuning the driving frequency and adapting the load resistance. The model can also be utilized as a means for further investigations, including the effect of material properties such as the piezoelectric strain coefficient and Young's modulus of the shim layer.

Declaration of conflicting interests

The author(s) declared no potential conflicts of interest with respect to the research, authorship, and/or publication of this article.

Funding

The author(s) disclosed receipt of the following financial support for the research, authorship, and/or publication of this article: This work was supported by the National Science Foundation ASSIST Nanosystems ERC under Award Number EEC-1160483.

ORCID iD

Binh Duc Truong https://orcid.org/0000-0001-7108-4713

References

- Annapureddy V, Kim M, Palneedi H, et al. (2016) Low-loss piezoelectric single-crystal fibers for enhanced magnetic energy harvesting with magnetoelectric composite. Advanced Energy Materials 6(24): 1601244.
- Annapureddy V, Na SM, Hwang GT, et al. (2018) Exceeding milli-watt powering magneto-mechano-electric generator for standalone-powered electronics. *Energy & Environmental Science* 11: 818–829.
- Arroyo E, Badel A, Formosa F, et al. (2012) Comparison of electromagnetic and piezoelectric vibration energy harvesters: model and experiments. *Sensors and Actuators A: Physical* 183: 148–156.
- Assawaworrarit S, Yu X and Fan S (2017) Robust wireless power transfer using a nonlinear parity-time-symmetric circuit. *Nature* 546: 387–390.
- Barman SD, Reza AW, Kumar N, et al. (2015) Wireless powering by magnetic resonant coupling: recent trends in wireless power transfer system and its applications. *Renewable and Sustainable Energy Reviews* 51: 1525–1552.
- Beeby SP, Tudor MJ and White NM (2006) Energy harvesting vibration sources for microsystems applications. *Measurement Science and Technology* 17(12): R175–R195.
- Bucciarelli L (2009) *Engineering Mechanics for Structures* (Dover Civil and Mechanical Engineering). New York: Dover Publications.
- Challa VR, Mur-Miranda JO and Arnold DP (2012) Wireless power transmission to an electromechanical receiver using low-frequency magnetic fields. *Smart Materials and Structures* 21(11): 115017.
- D'hulst R, Mitcheson PD and Driesen J (2006) CMOS buck-boost power processing circuitry for powerMEMS generators. In: *PowerMEMS 2006 technical digest*, Berkeley, CA, 29 November–1 December, pp. 215–218. Available at: http://cap.ee.ic.ac.uk/pdm97//powermems/2006/pdfs/215-218%20P43%20dhulst.pdf
- D'hulst R, Sterken T, Puers R, et al. (2010) Power processing circuits for piezoelectric vibration-based energy harvesters. *IEEE Transactions on Industrial Electronics* 57(12): 4170–4177.
- Erturk A and Inman DJ (2008a) On mechanical modeling of cantilevered piezoelectric vibration energy harvesters. *Journal of Intelligent Material Systems and Structures* 19(11): 1311–1325
- Erturk A and Inman DJ (2008b) Issues in mathematical modeling of piezoelectric energy harvesters. *Smart Materials and Structures* 17(6): 065016.
- Erturk A and Inman DJ (2009) An experimentally validated bimorph cantilever model for piezoelectric energy

harvesting from base excitations. Smart Materials and Structures 18(2): 025009.

- Erturk A and Inman DJ (2011) *Piezoelectric Energy Harvesting*. Chichester: Wiley.
- Erturk A, Hoffmann J and Inman DJ (2009) A piezomagnetoelastic structure for broadband vibration energy harvesting. *Applied Physics Letters* 94: 254102.
- Garraud A, Jimenez JD, Garraud N, et al. (2014) Electrodynamic wireless power transmission to rotating magnet receivers. *Journal of Physics: Conference Series* 557: 012136.
- Garraud N, Alabi D, Chyczewski S, et al. (2018) Extending the range of wireless power transmission for bio-implants and wearables. *Journal of Physics: Conference Series* 1052: 012023
- Garraud N, Garraud A, Munzer D, et al. (2019) Modeling and experimental analysis of rotating magnet receivers for electrodynamic wireless power transmission. *Journal of Physics D: Applied Physics* 52(18): 185501.
- Gonzalez G (1996) Microwave Transistor Amplifiers: Analysis and Design. 2nd ed. Upper Saddle River, NJ: Prentice-Hall.
- Halvorsen E (2016) Optimal load and stiffness for displacement-constrained vibration energy harvesters. arXiv. Available at: https://arxiv.org/abs/1603.01909
- Halvorsen E, Le CP, Mitcheson PD, et al. (2013) Architecture-independent power bound for vibration energy harvesters. *Journal of Physics: Conference Series* 476(1): 012026.
- Han J, Hu J, Wang Z, et al. (2015) Enhanced performance of magnetoelectric energy harvester based on compound magnetic coupling effect. *Journal of Applied Physics* 117(14): 144502.
- Hassan Q, Khan A and Madani S (2017) Internet of Things: Challenges, Advances, and Applications (Chapman & Hall/ CRC Computer and Information Science Series). Boca Raton, FL: CRC Press.
- Heebl JD, Thomas EM, Penno RP, et al. (2014) Comprehensive analysis and measurement of frequency-tuned and impedance-tuned wireless non-radiative power-transfer systems. *IEEE Antennas and Propagation Magazine* 56(5): 131–148.
- Huang L, Hu AP, Swain A, et al. (2013) An overview of capacitively coupled power transfer—a new contactless power transfer solution. In: 2013 IEEE 8th conference on industrial electronics and applications (ICIEA), Melbourne, VIC, Australia, 19–21 June, pp. 461–465. New York: IEEE.
- IEEE C95.1-2005 (2006) IEEE standard for safety levels with respect to human exposure to radio frequency electromagnetic fields, 3 kHz to 300 GHz (Revision of IEEE Std C95.1-1991).
- IEEE C95.6-2002 (2002) IEEE standard for safety levels with respect to human exposure to electromagnetic fields, 0-3 kHz
- Jorge Nocedal SW (2006) Numerical Optimization (Springer Series in Operations Research). 2nd ed. New York: Springer.
- Khaligh A, Zeng P and Zheng C (2010) Kinetic energy harvesting using piezoelectric and electromagnetic technologies-state of the art. *IEEE Transactions on Industrial Electronics* 57(3): 850–860.

Kiani M and Ghovanloo M (2012) The circuit theory behind coupled-mode magnetic resonance-based wireless power transmission. *IEEE Transactions on Circuits and Systems I: Regular Papers* 59(9): 2065–2074.

- Kim J, Kim DH and Park YJ (2015) Analysis of capacitive impedance matching networks for simultaneous wireless power transfer to multiple devices. *IEEE Transactions on Industrial Electronics* 62(5): 2807–2813.
- Kim YY and Kim JE (2011) Analysis of piezoelectric energy harvesters of a moderate aspect ratio with a distributed tip mass. *Journal of Vibration Acoustics Stress and Reliability* in Design 133: 041010.
- Kong CS (1995) A general maximum power transfer theorem. *IEEE Transactions on Education* 38(3): 296–298.
- Kurs A, Karalis A, Moffatt R, et al. (2007) Wireless power transfer via strongly coupled magnetic resonances. *Science* 317(5834): 83–86.
- Li J, Li M, Mu X, et al. (2018) Temperature and magnetic field dependencies of the Young's modulus in magnetostrictive Fe-Ga alloys. *Journal of Applied Physics* 123(7): 075102.
- Liao Y and Sodano H (2018) Optimal power, power limit and damping of vibration based piezoelectric power harvesters. Smart Materials and Structures 27(7): 075057.
- Liu G and Dong S (2014) A magneto-mechano-electric coupling equivalent circuit of piezoelectric bimorph/magnets composite cantilever. *Journal of Applied Physics* 115(8): 084112.
- Luo J, Flewitt A, Spearing S, et al. (2004) Young's modulus of electroplated Ni thin film for MEMS applications. *Materials Letters* 58(17): 2306–2309.
- Mitcheson PD, Yeatman EM, Rao GK, et al. (2008) Energy harvesting from human and machine motion for wireless electronic devices. *Proceedings of the IEEE* 96(9): 1457–1486.
- Moss SD, Payne OR, Hart GA, et al. (2015) Scaling and power density metrics of electromagnetic vibration energy harvesting devices. *Smart Materials and Structures* 24(2): 023001.
- Orfanidis SJ (2016) Electromagnetic Waves and Antennas.
 Online ed. Piscataway, NJ: ECE Department, Rutgers University. Available at: http://eceweb1.rutgers.edu/~orfanidi/ewa/
- Pacini A, Costanzo A, Aldhaher S, et al. (2017) Load- and position-independent moving MHz WPT system based on GaN-distributed current sources. *IEEE Transactions on Microwave Theory and Techniques* 65(12): 5367–5376.
- Paprotny I, Xu Q, Chan WW, et al. (2013) Electromechanical energy scavenging from current-carrying conductors. *IEEE* Sensors Journal 13(1): 190–201.
- Paul K and Sarma AK (2018) Fast and efficient wireless power transfer via transitionless quantum driving. *Scientific Reports* 8: 4134.
- Popovic Z, Falkenstein EA, Costinett D, et al. (2013) Low-power far-field wireless powering for wireless sensors. *Proceedings of the IEEE* 101(6): 1397–1409.
- Rao SS (2010) Mechanical Vibrations. 5 ed. Upper Saddle River, NJ: Prentice Hall.
- Renaud M, Elfrink R, Jambunathan M, et al. (2012) Optimum power and efficiency of piezoelectric vibration energy harvesters with sinusoidal and random vibrations. *Journal of Micromechanics and Microengineering* 22(10): 105030.

Renno JM, Daqaq MF and Inman DJ (2009) On the optimal energy harvesting from a vibration source. *Journal of Sound and Vibration* 320(1–2): 386–405.

Roundy S and Wright PK (2004) A piezoelectric vibration based generator for wireless electronics. *Smart Materials and Structures* 13(5): 1131–1142.

Sample AP, Meyer DT and Smith JR (2011) Analysis, experimental results, and range adaptation of magnetically coupled resonators for wireless power transfer. *IEEE Transactions on Industrial Electronics* 58(2): 544–554.

Shu YC, Lien IC and Wu WJ (2007) An improved analysis of the SSHI interface in piezoelectric energy harvesting. Smart Materials and Structures 16(6): 2253–2264.

Song M, Belov P and Kapitanova P (2017) Wireless power transfer inspired by the modern trends in electromagnetics. *Applied Physics Reviews* 4(2): 021102.

Tilmans HAC (1996) Equivalent circuit representation of electromechanical transducers: I. Lumped-parameter systems. *Journal of Micromechanics and Microengineering* 6: 157–176.

Truong BD and Roundy S (2018) Wireless power transfer system with center-clamped magneto-mechano-electric (MME) receiver: model validation and efficiency investigation. *Smart Materials and Structures* 28(1): 015004.

Truong BD (2019) Investigation on power optimization principles for series-configured resonant coupled wireless power transfer systems. *AEU: International Journal of Electronics and Communications* 106: 67–81.

Vittoz E (2010) Low-Power Crystal and MEMS Oscillators: The Experience of Watch Developments (Integrated Circuits and Systems). Dordrecht: Springer.

Wei C and Jing X (2017) A comprehensive review on vibration energy harvesting: modelling and realization. *Renewable and Sustainable Energy Reviews* 74: 1–18.

Zhu C, Leung VCM, Shu L, et al. (2015) Green internet of things for smart world. *IEEE Access* 3: 2151–2162.

Appendix I

Cases I, II and III: a comparison

Figure 14 gives us a bigger picture than the first two cases with a wide frequency range. We note that when the input frequency is far away from ω_0 and ω_1 , the optimal load can be approximated by $R_{\text{off}}^{\text{opt}} = 1/(\omega C_0)$.

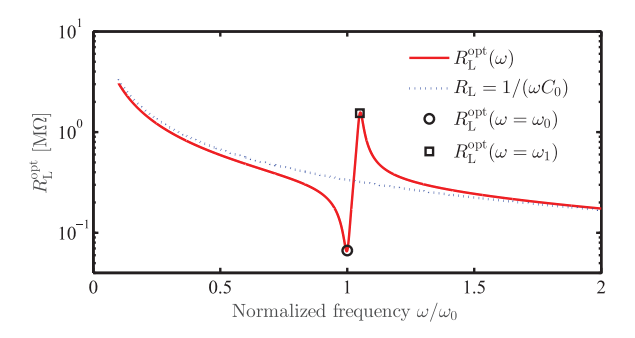


Figure 14. General solution of the optimal load as a function of the drive frequency, the other parameters are taken from Table 1.

This analysis can also be applied for non-resonant transducers.

Appendix 2

Case IV: optimal frequency as a function of load resistance

Figure 15 presents the changes of the optimal frequency when the load varies from 1 Ω to 100 M Ω . It is to be expected that the optimal frequency of high resistances approaches the anti-resonance (i.e. open-circuit resonant frequency) and that of low resistances tends to coincide with the resonant (short-circuit) frequency. However, when $R_L \in [100 \, \mathrm{k}\Omega, 5 \, \mathrm{M}\Omega]$ roughly, the optimal frequency is in between $f_0 = \omega_0/(2\pi)$ and $f_1 = \omega_1/(2\pi)$ and is given by formula (28). Once again, the model predicts exactly where the drive frequency should be for the specific load used in the experiments.

Appendix 3

Case V: numerical solutions

Figure 16 presents the optimum power at each driving frequency with the corresponding optimal load given by equation (26). The global maximum output power is achieved either at $\omega_{\rm M_1}$ or $\omega_{\rm M_2}$, while a local minimum is observed at $\omega_{\rm m}$. Given the facts that asynchronously switched electronic interfaces (e.g. buck-boost converters) can be utilized as an effective load resistance (i.e. by tuning the duty cycle of the switching circuit; D'hulst et al., 2006, 2010) and the driving frequency of a WPT system is able to be adjusted easily, the exact solutions presented in this section offer a convenient means for realizing an optimal system in practice.

In order to check the accuracy of the analytical calculation procedure, we also develop a numerical approach to solve the general power optimization problem ($Case\ V$) based on equation (21). It is formulated as follows

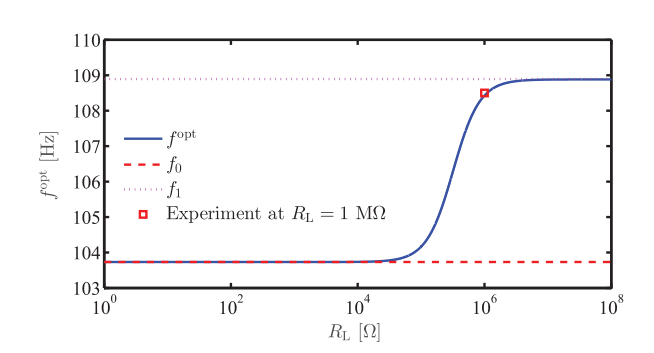


Figure 15. General solution of the optimal frequency for an arbitrary load resistance.

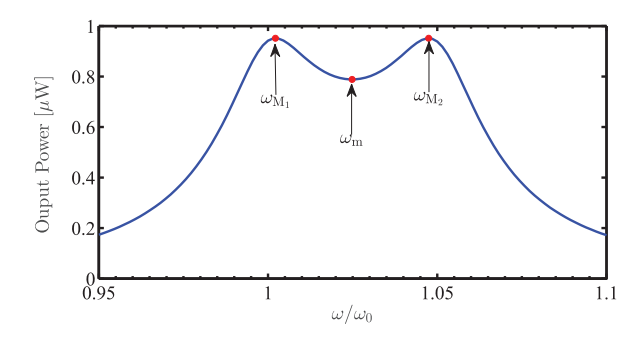


Figure 16. Maximum transferred power as a function of the driving frequency and the optimal load calculated by equation (26). Solid dot: analytical solutions of the optimal frequencies (equations (37) to (39)).

$$\max_{\omega,\tau} P \text{ subject to } \omega > 0, \ \tau > 0. \tag{76}$$

To deal with such a nonlinear optimization problem with inequality constraints, the nonlinear Interior Point and Sequential Quadratic Programming methods can be used (Jorge Nocedal, 2006). The numerical solutions are exactly the same as those obtained from analytical closed form, showing that the optimal loads and frequencies are either close to but not necessarily identical to *Cases I and II*. The differences between them are strongly dependent on system parameters such as beam geometry, parasitic damping coefficient, and transduction factor.

Figure 17 shows two normalized numerical solutions of the general power optimization problem addressed in equation (76), note that $\omega_1/\omega_0=1.05$. Here, we denote $R_{\rm L}^0$ and $R_{\rm L}^1$ as the loads expressed in equations (22) and (24), respectively. With the particular prototype used for these measurements, the optimal solutions of *Case V* are not so different from those of *Cases I* and *II*. Therefore, the obtained power outputs of three mentioned cases are considerably indistinguishable. This indicates that for practical convenience, either ω_0 or ω_1 can be used to drive moderately coupled systems, while the load is optimized to maximize the output power.

However, we mathematically point out an example shown in Figure 18 where the maximum powers given by equations (23) and (25) are more clearly different from the solution of equation (76). Pseudo parameters b_s , t_{p-s} , L_s , Γ_s are set for simulations by multiplying the actual ones (in Table 1) with a chosen factor as seen in Figure 18. The aim of this study is to realize that the resonant/anti-resonant frequencies are not always the optimal value, which depends on particular system

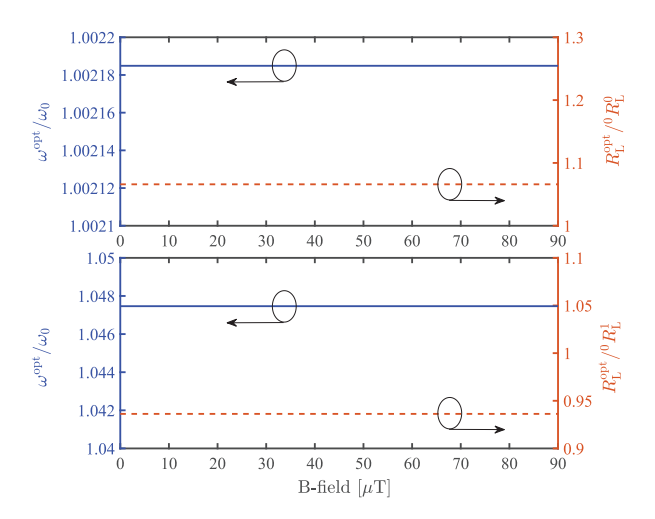


Figure 17. Numerical solutions of the optimal load and frequency, which is independent on the applied **B** field.

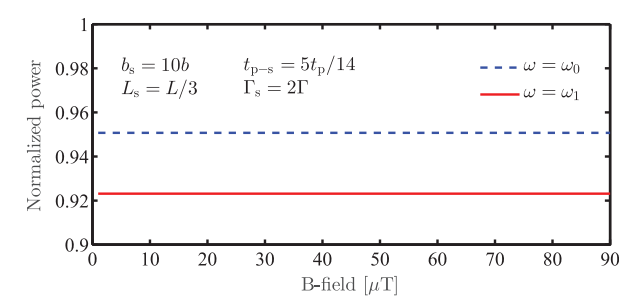


Figure 18. An example indicates the difference when the power obtained from *Cases I* and *II* are compared to that of *Case V*.

parameters. Finally, it should be noted that all theoretical results reported in this article can be independently affirmed by dynamic simulations using SPICE simulators.

While the particular beam used in these measurements only generated a few μ W, the power density was about 152 μ W/cm³ at $B_{ac} = 300 \,\mu$ T, which is typical with the use of piezoelectric technologies (Khaligh et al., 2010; Moss et al., 2015) and is comparable to that of far-field wireless powering systems (Popovic et al., 2013). Furthermore, our simulations indicate that if we double the magnet volume and halve the length of the piezoelectric cantilever, the power density could be significantly higher, with a factor of ~3.8 potential improvement.